OneTouch Automated Photoacoustic and Ultrasound Imaging of Breast in Standing Pose

Huijuan Zhang, Emily Zheng, Wenhan Zheng, Chuqin Huang, Yunqi Xi, Yanda Cheng, Shuliang Yu, Saptarshi Chakraborty, Ermelinda Bonaccio, Kazuaki Takabe, Xinhao C. Fan, Wenyao Xu, *Senior Member, IEEE*, and Jun Xia, *Member, IEEE*

***Abstract*— We developed an automated photoacoustic and ultrasound breast tomography system that images the patient in the standing pose. The system, named OneTouch-PAT, utilized linear transducer arrays with optical-acoustic combiners for effective dual-modal imaging. During scanning, subjects only need to gently attach their breasts to the imaging window, and co-registered three-dimensional ultrasonic and photoacoustic images of the breast can be obtained within one minute. Our system has a large field of view of 17 cm by 15 cm and achieves an imaging depth of 3 cm with sub-millimeter resolution. A three-dimensional deep-learning network was also developed to further improve the image quality by improving the 3D resolution, enhancing vasculature, eliminating skin signals, and reducing noise. The performance of the system was tested on four healthy subjects and 61 patients with breast cancer. Our results indicate that the ultrasound structural information can be combined with the photoacoustic vascular information for better tissue characterization. Representative cases from different molecular subtypes have indicated different photoacoustic and ultrasound features that could potentially be used for imaging-based cancer classification. Statistical analysis among all patients indicates that the regional photoacoustic intensity and vessel branching points are indicators of breast malignancy. These promising results suggest that our system could significantly enhance breast cancer diagnosis and classification.**

***Index Terms*— Photoacoustic imaging, ultrasound, breast cancer.**

Received 4 April 2025; revised 17 May 2025; accepted 9 June 2025. Date of publication 12 June 2025; date of current version 30 October 2025. This work was supported by the National Institute of Health under Grant R01EB029596, Grant R01EB028978, and Grant R01EB035188. Recommended by Associate Editor C. Kim. *(Corresponding author: Jun Xia.)*

This work involved human subjects or animals in its research. Approval of all ethical and experimental procedures and protocols was granted by the Institutional Review Board of the Roswell Park Comprehensive Cancer Center and the University at Buffalo.

Huijuan Zhang, Emily Zheng, Wenhan Zheng, Chuqin Huang, Yunqi Xi, Yanda Cheng, and Jun Xia are with the Department of Biomedical Engineering, University at Buffalo, The State University of New York, Buffalo, NY 14260 USA (e-mail: huijuanz@buffalo.edu; emilyzhe@buffalo.edu; wzheng26@buffalo.edu; chuqinhu@buffalo.edu; yunqixi@buffalo.edu; yandache@buffalo.edu; junxia@buffalo.edu).

Shuliang Yu and Saptarshi Chakraborty are with the Department of Biostatistics, University at Buffalo, The State University of New York, Buffalo, NY 14214 USA (e-mail: shuliang@buffalo.edu; chakrab2@buffalo.edu).

Ermelinda Bonaccio is with the Department of Breast Imaging, Roswell Park Comprehensive Cancer Center, Buffalo, NY 14203 USA (e-mail: Ermelinda.Bonaccio@RoswellPark.org).

Kazuaki Takabe is with the Department of Surgery, Roswell Park Comprehensive Cancer Center, Buffalo, NY 14203 USA (e-mail: Kazuaki.Takabe@RoswellPark.org).

Xinhao C. Fan is with the Windsong Radiology, Buffalo, NY 14226 USA (e-mail: XFan@windsongwny.com).

Wenyao Xu is with the Department of Computer Science and Engineering, University at Buffalo, The State University of New York, Buffalo, NY 14260 USA (e-mail: wenyaoxu@buffalo.edu).

This article has supplementary downloadable material available at https://doi.org/10.1109/TMI.2025.3578929, provided by the authors.

Digital Object Identifier 10.1109/TMI.2025.3578929

I. Introduction

BREAST cancer is a major global health concern, with 2.26 million new cases diagnosed in 2020. It is a leading cause of death among women, with approximately 684,996 women losing their lives to the disease around the world in 2020 [1], [2]. As the evidence shows, early detection has significantly reduced mortality rates, with the female breast cancer death rate falling by 41% in the US since 1989 [3]. While current diagnostic methods, such as X-ray mammography, ultrasound imaging, and magnetic resonance imaging (MRI), have vastly improved over the past decades, they still have limitations that compromise accuracy or availability. For example, X-ray mammograms involve painful breast compression and have lower sensitivity in dense breast tissue [4], [5]. While digital tomosynthesis and contrast-enhanced mammography improve detection sensitivity for patients with high breast density, they are either associated with a high radiation dosage [6] or need contrast injection [7]. MRI, on the other hand, is expensive, time-consuming, and not universally available [8], [9]. Finally, handheld ultrasound has high false-positive rates and is subject to operator variability [10]. To address these limitations, there is a need for more accurate breast cancer screening methods, particularly for radiographically dense breasts [10], [11]. Automated Photoacoustic (PA) tomography (PAT) and ultrasound (US) are promising dual-modality techniques to overcome many of these limitations [12], [13], [14].

The PA effect refers to the process of converting light energy into sound. Its discovery dates back to the late 1800s [15]. The mechanism involves using a short-pulsed laser to provide excitation light, which is absorbed by molecules such as hemoglobin, lipid, or melanin. This absorption leads to thermoelastic expansion and the generation of acoustic waves that propagate through the tissue [16]. Ultrasound transducer arrays detect these acoustic waves, and the received signals are used to reconstruct an image of the distribution of optical absorbers [17], [18]. The photoacoustic technique combines the benefits of high optical absorption contrast and high acoustic resolution, making it a valuable tool for breast cancer imaging [19]. Most PA breast imaging systems utilize near-infrared wavelengths, which provide a good balance between

blood absorption and tissue penetration [20], [21], [22]. The acquired hemoglobin map can help to identify tissue malignancy [23], [24]. In general, breast cancer tissue contains more hemoglobin than benign abnormalities or normal tissue, likely due to tumor angiogenesis [25], [26]. The use of PAT to evaluate these additional tumor features could reduce the need for unnecessary biopsies [27], assist in diagnosing breast cancer [28], [29], [30], and support the monitoring of therapies and drug development [31].

Over the past decade, using the photoacoustic principle for breast cancer imaging has become increasingly prevalent [12], [23], [32]. Many of the existing systems require the patient to be in a prone position, which has the drawback of requiring larger clinical space and longer imaging preparation time. In addition, most of these systems do not have native ultrasound imaging capability. For example, the Twente PAM 2 [33] and SBH-PACT [28] systems provided 3D vasculature images of the breast, but both lacked ultrasound data for structural analysis of the lesion. The PAI-04 [34] and LOUISA-3D [35] systems provided both PA and US images. However, the two modalities were captured by two different transducers with different fields of view and spatial resolutions. There are also systems that image patients in a supine pose and offer dual-modal PA and US imaging using the same transducer. For example, the Imagio system uses hand-probe linear arrays to simultaneously acquire PA and US data [27], [36]. However, the handheld imaging scheme is operator-dependent and cannot provide volumetric features for comprehensive 3D tumor information.

Our group previously developed a photoacoustic dual-scan mammoscope (DSM) system that used two linear transducer arrays to scan the breast in a craniocaudal view, providing naturally co-registered volumetric PA and US images with the patient in standing position [21], [29], [37]. However, this system works better in breasts with large cup sizes. Additionally, although the system delivers cranio-caudal images similar to a mammogram, many patients have preferred a method that does not require compression. To overcome this limitation, we propose an upgraded design that provides a frontal view of the breast with minimal compression.

The OneTouch-PAT system builds upon the advantages of the DSM by maintaining an upright imaging position and providing co-registered PA/US images, while accommodating a wider range of breast sizes. The system offers a simple and comfortable imaging process, requiring patients to gently attach their breast to the imaging window, where a U-shaped scanning transducer array captures high-resolution 3D PA/US images within approximately one minute over a 17 cm $\times$ 15 cm field of view. A clinical study was conducted involving 61 patients to demonstrate the OneTouch-PAT system's ability to visualize the tumor features in both PA and US images and provide statistically significant differences in vascular intensity and distribution between malignant and healthy breast tissue.

II. Methods

A. System Configuration

The OneTouch-PAT consists of a portable laser, a water tank with an imaging window in the front, a height-adjustable lift table, and two linear scanning stages. The imaging window is sealed with a 0.002-inch thick clear plastic film that ensures both acoustic and light transmission. The schematic of the system is displayed in **Figure 1a**. The imaging platform was secured on an optical breadboard, which was fixed to a mobile lift table with an adjustable height. The water tank had a depth of 13 cm, a width of 25 cm, and a height of 20 cm. This design provided space for the imaging probe to move freely in the water tank. The transducer and optical fiber bundle were combined using a compact double-reflector design with two dichroic mirrors mounted at 45 degrees, allowing for co-planar illumination and acoustic detection [38]. A close-up view of the imaging cross-section is provided in **Figure 1b**. The combined transducer and fiber bundle were placed into the water tank and connected to two motorized translation stages through T-slotted aluminum frames. The scanning was controlled by an Arduino board, which was programmed to synchronize with the laser firing.

The ultrasound transducer used for both PA and US acquisition was a custom-made 128-element linear array (Imasonic, Inc.) with 86-mm lateral length, 2.25 MHz central frequency, and $>65\%$ bandwidth. Each element had an arc-shaped aperture with 40 mm elevation focusing, 15 mm element height, and 0.67 mm pitch. The long elevation focus allows optimal acoustic performance across the scanning. The light source was a compact Nd: YAG laser (Quantel model CFR400) with 1064 nm output, 20 Hz pulse repetition rate, and 10 ns pulse width. The laser beam was fed to a fiber bundle with line output. The laser fluence on the skin was approximately 40 mJ/cm^2, which was within the safe limits for laser exposure specified by the American National Standards Institutes (ANSI) (100 mJ/cm^2 at 1064 nm) [39]. To synchronize the OneTouch-PAT system, we used the laser's reference output to trigger both the data acquisition systems and the linear translation stages. The Verasonics Vantage data acquisition (DAQ) system was utilized for both PA and US data acquisition. The acquired raw data was reconstructed and processed in MATLAB. As the One-touch system shared the same transducer and light delivery scheme of DSM, it has the same lateral resolution of 1 mm and elevation resolution of 1 to 2 mm [21], which can be further improved by the methods mentioned below.

B. Imaging Procedure

Before imaging, the patient stood upright and was instructed to lean forward to gently attach one breast to the imaging window. Both breast and imaging windows will be pre-applied with green ultrasound gel (Parker Laboratories, Inc.) to ensure optimal coupling. To ensure patient comfort, the water tank was filled with warm, distilled water. The patient will be instructed to raise the arm on the side being imaged to better expose the breast tissue. A raised bar attached to the imaging platform will be available for the patient to hold, enhancing comfort during the procedure. During imaging, the OneTouch-PAT system utilizes a round-trip scanning procedure to achieve a field of view of 17cm $\times$ 15 cm. The scanning process involves three steps. First, the transducer starts at the bottom left side of the breast and scans upward at 8 mm/s over 17 cm (**Figure 1c**). Second, the scanning switches to the

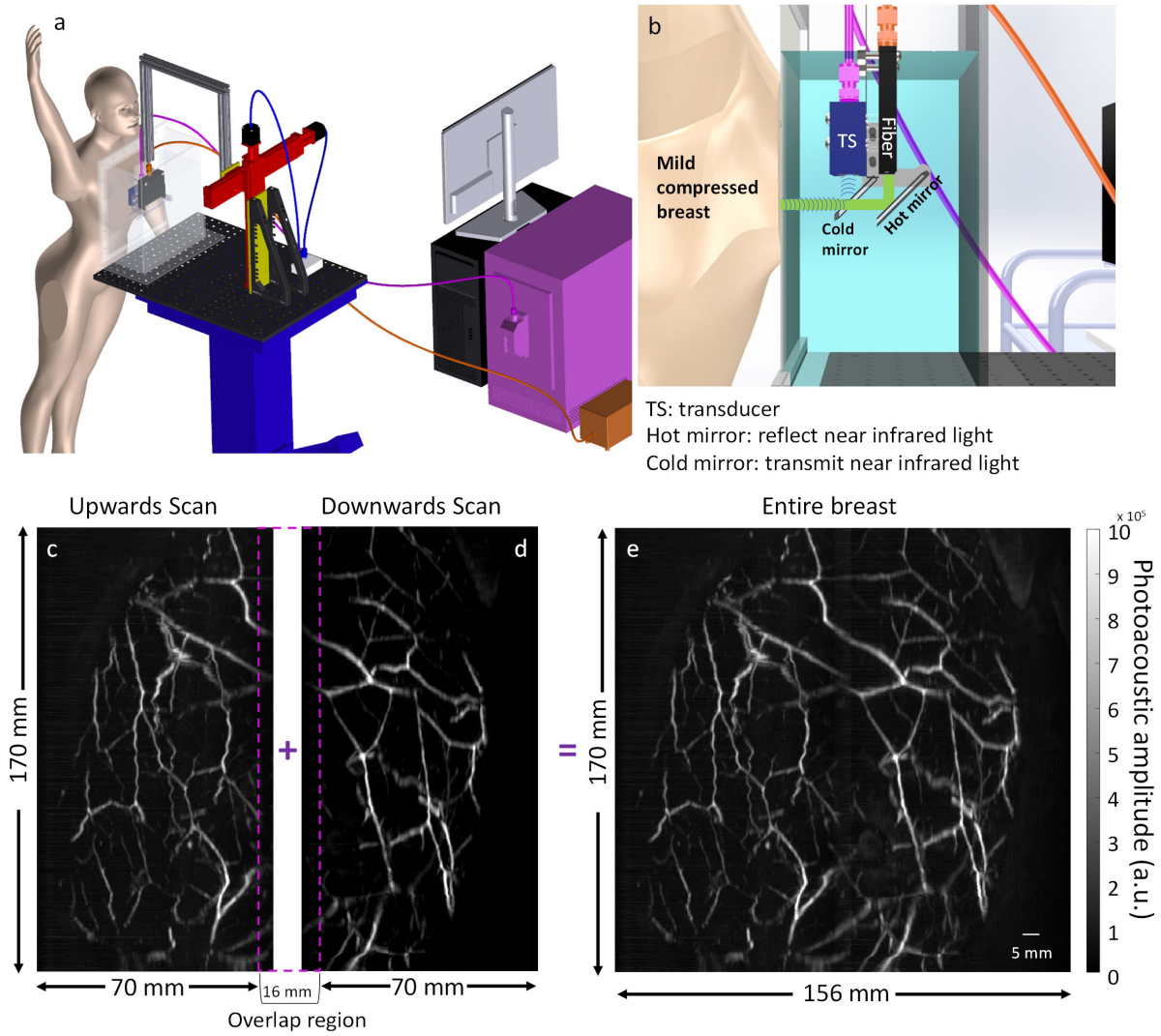

Fig. 1. Top row: a, schematic drawing of the OneTouch-PAT system. b, zoom-in image of the double-reflector design for coplanar illumination and acoustic detection. After accounting for acoustic reflection, the distance from the transducer to plastic film ranges from 30 to 35 mm. The transducer focuses at 40 mm. Bottom row: c, PA image from the upward scan. The transducer scanned from the bottom left corner of the water tank up over 17 cm. d, PA image from the downward scan. After the upward scan, the transducer laterally moved 7 cm and then scanned down over 17cm. The purple dashed box marked the overlapped region between the two scans. e, the combined PA image from two scans. The breast images are presented in frontal view.

second translation stage to perform a 7-cm horizontal shift to the right. Finally, the transducer scans downward to cover the right side of the breast (**Figure 1d**). The scanning results are combined to form the final imaging data (**Figure 1e**). A single round-trip scanning takes approximately 52 seconds to complete.

C. High-Performance Ultrasound Imaging

Multi-angle wide-beam imaging strategies were implemented to obtain high-quality US images. Based on the same transducer, a wide-beam transmit sequence was used to send US waves at three different steering angles (−15°, 0°, and 15°), with 42 wide-beam transmissions per angle across the lateral length of the transducer. This large number of transmit beams reduces side lobe levels in the US image, allowing for high-quality US without sacrificing acquisition time. The data were spatially compounded and averaged to form a single US frame. Stacking the cross-sectional B-mode US image along the scanning direction creates a 3D volumetric US image of the breast tissue. Compared to the multi-angle plane imaging approach in our previous DSM system, the wide-beam imaging process provided better US image quality and can reveal more details of the breast tissue [29].

D. Photoacoustic Data Acquisition and Processing

As PA signals are much weaker than pulse-echo US, they have a low signal-to-noise ratio. To further enhance the signals, we added a 128-channel 40-dB preamplifier (Legion AMP, Photosound Technologies) to the Verasonics system. The preamplifier could not handle ultrasound firing, so PA and US were performed separately. The patient remained still in front of the imaging window during PA and US scans (each takes 1 minute). This allows the system to acquire both PA and US data at the same position. To ensure accurate registration of PA and US images, we record key anatomical landmarks, including the compressed breast tissue

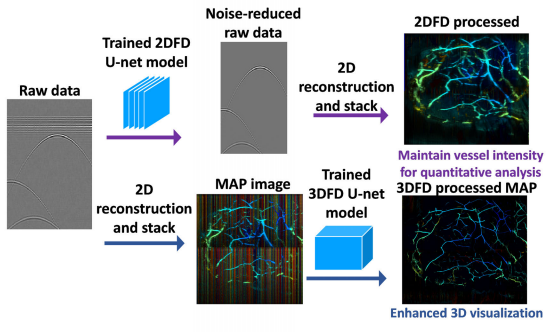

Fig. 2. The flowchart of the breast data processing. Top row: a 2DFD U-net model was used to remove the experimental noise from the raw data. The raw data frames were then reconstructed and stacked to form a max amplitude projection (MAP) image. This method preserves the original signal intensity for quantitative analysis. Bottom row: the raw data frames were reconstructed and stacked to form a 3D volume. The trained 3DFD U-net model was then applied to the volume to enhance the 3D vasculature. This method provides better visualization of blood vasculature.

shape, nipple location, and the tumor regions during the two scans. During the image fusion, we align the breast tissue outlines and verify that the nipple positions match in both PA and US images. In most of our patient studies, no adjustments were needed to align the PA and US images.

Noises from PA imaging include thermal noise and electromagnetic interference (EMI) noise from laser firing. Both will contaminate the true PA signals. Additionally, the poor elevational resolution of linear arrays along the scanning direction will degrade the 3D vascular images [40]. To address these challenges, two deep learning networks were built for OneTouch-PAT.

One 2D fully-dense Unet (2DFD) was utilized to denoise the raw channel data before image reconstruction. The 2DFD architecture was the same as in our previous publication [41], except that this study focuses on noise removal instead of resolution improvement. During training, we fed the network with simulated data added with experimentally acquired system noise. This allows the network to learn the noise characteristics of the imaging setup. After training, the network was applied to the experimental breast data to remove noise. Since only noise was removed from the processing, this method can maintain the original vessel intensity for quantitative analysis.

For better visualization of the 3D vessel structure, we also incorporated our recently developed 3D fully-dense (3DFD) Unet [42], which will enhance vessel structure and improve vessel continuity. The 3DFD processed data was used for vessel visualization and branching point analysis.

The two data processing approaches are shown in **Figure 2** for comparison. The first row shows the 2DFD model. The second row indicates the data processing procedure for 3DFD Unet. The 3D-trained networks can better preserve the vascular structure in the 3D space by exploring the data's volumetric information rather than cross-sectional images. Meanwhile, the overall image quality was improved as imaging artifacts and noises were further removed. It should be noted that the 3DFD Unet training already incorporated system noise into training. Therefore, we did not use the 2D FD-Unet processed data as input for the 3DFD Unet [42].

E. Tumor Analysis

We began by comparing our ultrasound images with the clinical US report to identify morphologically similar lesions in our data. Once we identified the relevant frame numbers in the experimental US images, we examined the corresponding PA vascular features around the tumor region. Next, we conducted a quantitative analysis that included quantification of vessel contrast, average vessel signal intensity, vessel branching points, and standard deviation of vessel and background. The statistical analysis was then done by comparing these features with the results of the healthy contralateral breast.

Most of the quantitative analysis was performed on the 2DFD data, except for the branching point which calculated from the 3DFD data. To identify the branching points, we used the MATLAB function "bwmorph" to detect branching points from the maximum intensity projection (MIP) image. To eliminate false positives caused by overlapping vessels at different depths, the detected 2D points were further validated in 3D by analyzing their local neighborhoods within the volumetric data. Points without sufficient 3D continuity were excluded from the analysis. The branching point density was calculated by dividing the total number of branching points by the total breast area in the projection image.

F. Human Subject Recruitment

Human experiments in this study were approved by the Institutional Review Board of the Roswell Park Comprehensive Cancer Center and University at Buffalo, which also overlooked patient imaging studies conducted at Windsong Radiology. All human subjects provided informed consent after fully understanding the implications of their participation. Windsong patients were recruited by patient navigators, while Roswell Park patients were recruited by study nurses and breast surgeons. The entire imaging procedure for both breasts takes less than 10 minutes. The study enrolled four healthy volunteers from University at Buffalo. The healthy volunteer study aimed to test the performance of the OneTouch-PAT system in different cup sizes and verify the reliability of the deep learning data processing method. After that, 61 patients diagnosed with breast cancer participated in the clinical testing. The comprehensive characterization of the patient information is listed in Table I. Results from five patients were selected to demonstrate the dual-modal PA/US imaging capabilities, while all patients' PA results were used for the statistical analysis.

III. Results

The results are presented in three sections. First, we evaluated OneTouch-PAT on four healthy subjects with varying breast sizes and skin tones, demonstrating its robustness across different breast compositions using optimized data processing algorithms. Next, a clinical validation study was conducted, showing that OneTouch-PAT enables clear visualization of tumor features in both 2D and 3D data. Finally, a quantitative analysis of 61 patients revealed that photoacoustic imaging provides statistically significant differences in signal intensity and vessel distribution between malignant and healthy breast tissue.

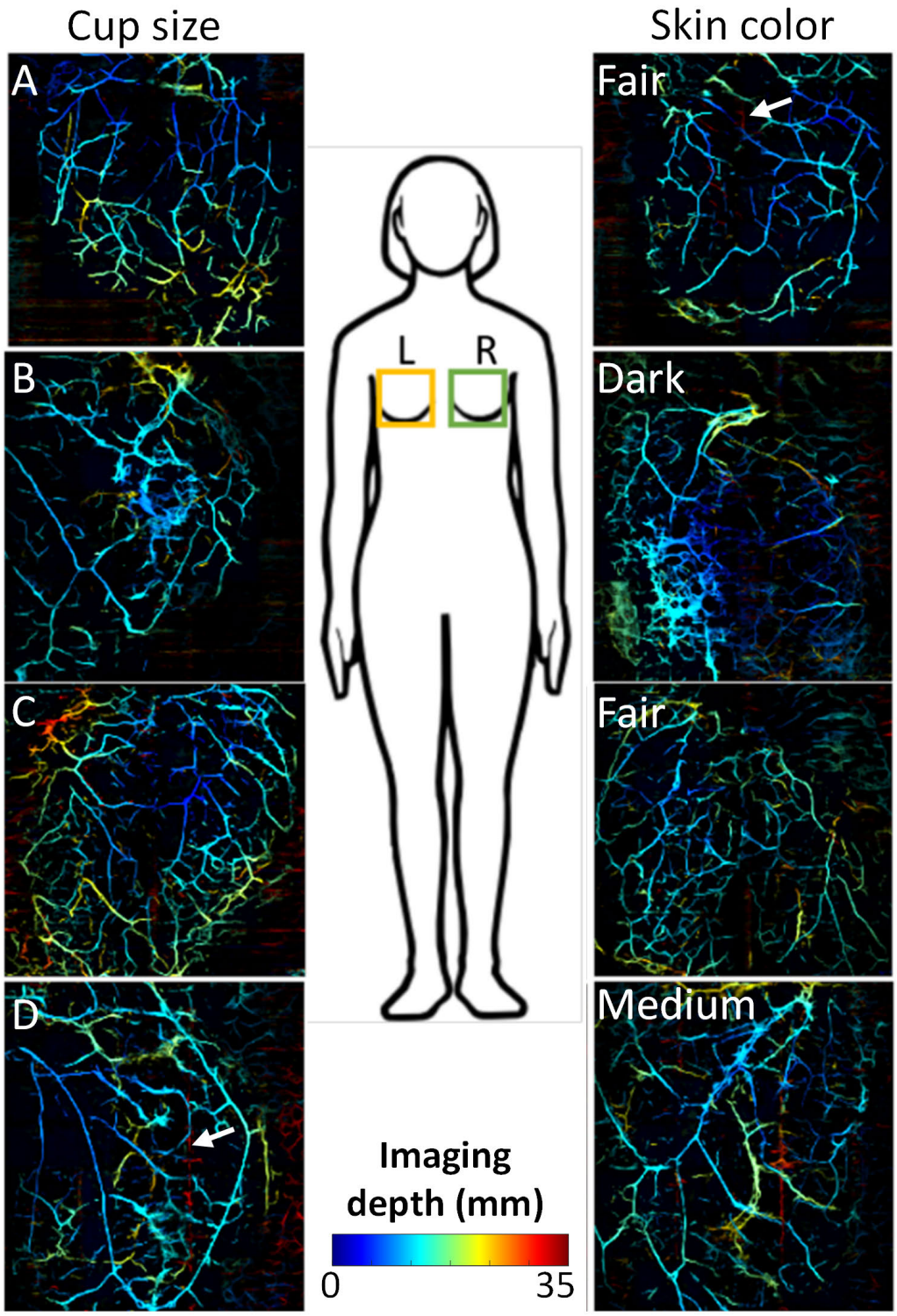

Fig. 3. Depth-encoded MAP images of breast vasculature from four healthy volunteers with cup sizes from A-D. The subjects also have different skin colors. Each row represents images of left and right breast from the same subject. The imaging field of view is 156 mm × 170 mm. The depth was quantified in reference to a planar surface close the plastic membrane. Vessels near 3 cm deep are seen in red colors and marked by white arrows.

A. Data Processing and Healthy Subject Results

Four healthy volunteers with different breast cup sizes and skin tones were recruited to demonstrate the system's performance. The results are shown in **Figure 3**, where images were projected along the axial direction and color-encoded with depth (blue represents shallow and red represents deep). The OneTouch-PAT system provides consistent imaging of blood vessels at different cup sizes. For instance, blood vessels can be clearly visualized at the top row of the small cup size A, as well as in the bottom row of cup size D. The

TABLE I
SUMMARY OF PATIENT DATA

Patient Data	No. of Patients
Total number of patients	61
Breast density	Almost entirely fatty (1) Scattered Fibroglandular Density (35) Heterogeneously Dense (23) Extremely Dense (2)
Ages	32-76
Tumor size range	≤10 mm (26) 10-30 mm (26) 30-70 mm (7) Unknown (2)
Tumor types	ILC (4) IDC and mixed (42) DCIS (11); LCIS (1); ADH (1) Unknow (2)
Molecular subtype	LUMA (26) LUMB (10) TNBC (6) Unknown (19)
Nottingham grade	1 (6) 1-2 (9) 2 (22) 3 (14) Unknown (10)
Skin color	Fair (49) Medium (4) Dark (8)
Breast cup size	A (4) B (13) C (13) D (31)

ILC: Invasive Lobular Carcinoma; IDC: Invasive Ductal Carcinoma; DCIS: Ductal Carcinoma In Situ; LCIS: Lobular Carcinoma In Situ; ADH: Atypical Ductal Hyperplasia. LUMA: Luminal A; LumB: Luminal B; TNBC: Triple-negative breast cancer.

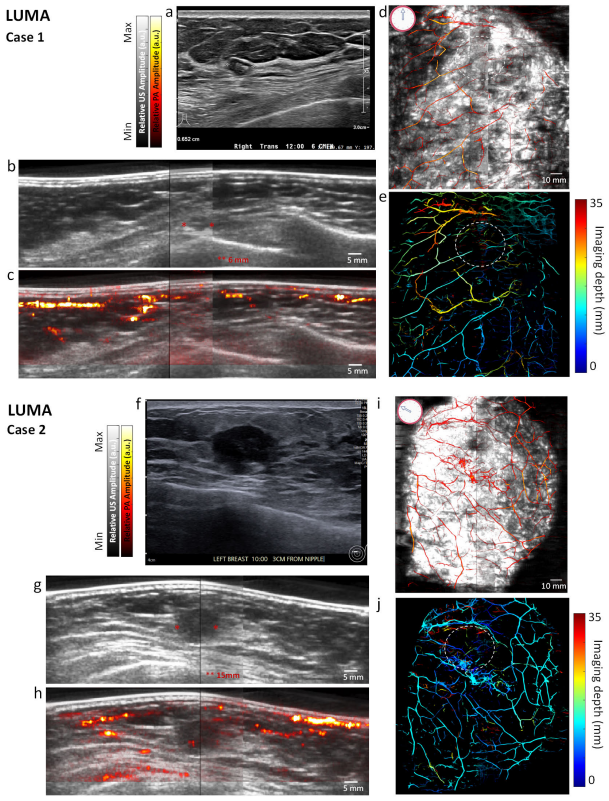

Fig. 4. OneTouch-PAT imaging results of two LUMA cases. a&f represent the clinical US images. b&g represent the one-touch US (gray) images. c&h represent the PA (color) images overlaid on top of grayscale US images. d&i represent the 3D projection PA overlaid on top of US images (frontal view of the breast). e&j represent the depth-encoded 3D projection PA images (frontal view of the breast). For the overlay images, the PA intensity was linearly mapped to a transparency matrix, with the strongest PA signals rendered completely opaque and the weakest signals fully transparent.

subject with a cup size of B has a dark skin color, which would provide a stronger background signal. The deep learning process eliminates most of the skin signals, thereby revealing deeper vascular features.

B. Patient Imaging Results

In this section, we present the morphological and vascular tumor features in 2D and 3D. Five representative cases are presented to cover three molecular subtypes of breast cancer: LUMA, LUMB, and TNBC.

Figure 4 displays PA&US results from two patients with LUMA breast tumors. Case 1 involved a patient with fair skin color and cup size C, having a $7 \times 5 \times 6$ mm^3 tumor (LUMA) on the right breast at 12 o'clock, 6 cm from the nipple. The clinical US report (**Figure 4a**) shows an oval-circumscribed hypoechoic mass with central echogenicity. The same feature is observed in the One-Touch US image (**Figure 4b**). **Figure 4c** presents the PA features overlaid on top of the cross-sectional US image where some blood vasculatures can be seen. However, the presence of the vessel is dependent on the orientation of the cross-section. In comparison, the 3D renderings in **Figure 4d** and **Figure 4e** show more peripheral vessels, highlighting the importance of volumetric imaging. It should be noted that the orange-red colored vessels at the top left corner of Figure 4e might be due to nature curvature of the breast as our plastic membrane was flexible and did not conform the breast to a flat surface.

The second LUMA case involved a patient with fair skin color and cup size D, having a $15 \times 15 \times 17$ mm^3 tumor on the left breast at 10 o'clock, 3 cm from the nipple. The clinical US image shows a lobulated, partially well-circumscribed, heterogeneously enhancing mass (**Figure 4f**), which is also visible in the One-Touch US image (**Figure 4g**). Similar to the first case, we noticed more obvious vascular patterns in the volumetric image than the cross-sectional images (**Figure 4h-j**). In both LUMA cases, we observed that the peripheral vessels of the tumor were more prominent than the internal vessels.

Figure 5 presents PA&US images of two patients (case 3&4) with LUMB subtype. In case 3, the patient (breast cup size A and fair skin color) has a $22 \times 18 \times 24$ mm^3 tumor behind the left nipple with overlying skin thickening. The clinical US image (**Figure 5a**) shows an irregular hypogenic lesion which matches with the One-Touch US image (**Figure 5b**). The PA cross-sectional and volumetric images in **Figure 5c-e** show richer vasculature around the tumor core.

In case 4, the patient (cup D breast and fair skin color) has a $32 \times 17 \times 19$ mm^3 spiculate mammographic mass in

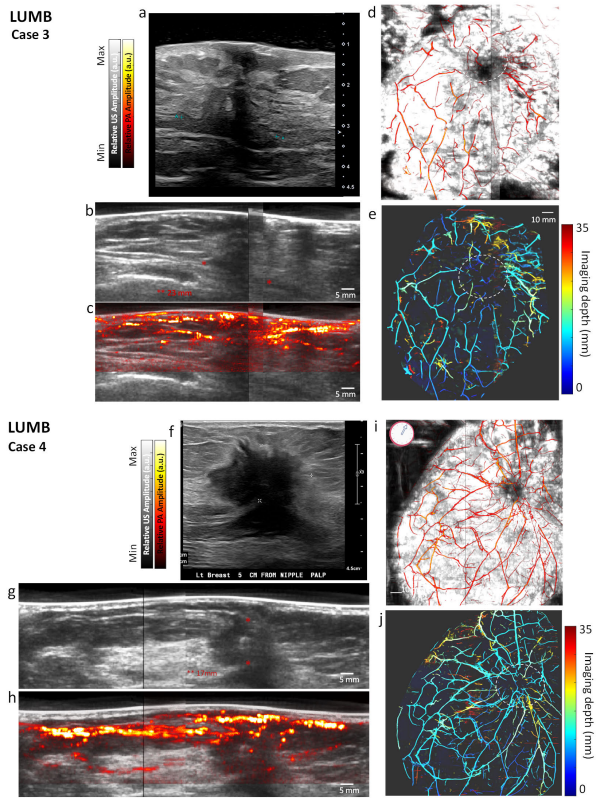

Fig. 5. OneTouch-PAT imaging results of two LUMB cases. a&f represent the clinical ultrasound image. b&g represent the one-touch ultrasound (gray) images. c, h represent the photoacoustic (color) images overlaid on top of US images. d&i represent the 3D projection PA overlaid on top of US images (frontal view of the breast). e&j represent the depth-encoded 3D projection PA images (frontal view of the breast).

the left breast. Again, a hypogenic lesion with an irregular shape is shown in both clinical (**Figure 5f**) and One-Touch US images (**Figure 5g**). The PA images show that the tumors have abundant vessels surrounding the periphery and fewer vessels in the central region (**Figure 5h-j**). In particular, compared to LUMA cases, we noted a more pronounced presence of feeding vessels leading to the tumor core in both LUMB cases. This vascular richness in LUMB tumors suggests a higher angiogenic activity, likely contributing to their higher proliferation rates and more aggressive tumor behavior, as indicated by their elevated Ki-67 indices. A 3D rendering of the PA and US image overlay is shown in Video 1 (Supplementary Material) (scale bar 2 cm).

Figure 6 illustrates the PA&US results of a malignant lesion of the TNBC subtype. Case 5 involved a patient with fair skin color and cup size C. The patient had a lobulated sonographic mass with indistinct margins located at 11 o'clock in the right breast, measuring 22 × 18 × 22 mm^3. Both clinical (**Figure 6a**) and One-Touch ultrasound (**Figure 6b**) images revealed a ∼20 mm lesion with a circumscribed margin and round shape; both are characteristic features of TNBC [43]. Within the tumoral region, we observed spotty high-intensity photoacoustic signals (**Figure 6c**), which are likely attributed to intertumoral hemoglobin enhancement. Interestingly, we did not observe clear feeding vessels in this TNBC case (**Figure 6d-e**), potentially due to the lack

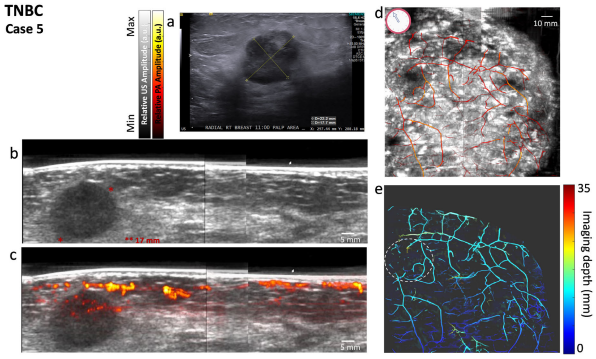

Fig. 6. OneTouch-PAT imaging result of a TNBC case. a represents the clinical ultrasound image. b represents the one-touch ultrasound (gray) image. c represents the photoacoustic (color) image overlaid on top of the US image. d represents the 3D projection PA overlaid on top of the US image (frontal view of the breast). e represents the depth-encoded 3D projection PA image (frontal view of the breast).

of ER and HER2 expression, which created a less structured vascular network [44].

C. Statistical Analysis

Statistical analysis was conducted using MATLAB with a type I error rate of 0.05 (α). Upper-tailed t-tests were utilized to compare different parameters for healthy and tumor-bearing breasts. Based on our earlier study on the DSM system [29], we analyzed the regional PA intensity (Ave Intensity), the background PA intensity (Ave Background), the standard deviation of the background PA intensity (STD Background), and the extracted vessel intensity (Ave Vessel) across 61 patients (Table II). The data from the tumor-bearing breast was normalized by dividing it by the corresponding data from the healthy breast. **Figure 7** provides a summary of our statistical results.

As shown in **Figure 7a**, the malignant breasts exhibit higher relative photoacoustic intensity (> 1) compared to the healthy breasts. Our analysis revealed that tumor-bearing breasts exhibited stronger regional signal intensity ($P = 0.0002$ for upper tailed t-test) and vessel intensity ($P = 0.0062$) than healthy breasts. This finding suggests the presence of larger vessels and abundant microvessels in malignant breasts. This observation is consistent with current research that indicates an increase in regional vascularity in malignant breasts [45], [46]. Additionally, mean signal intensity of the background (regions with no visible vessel) ($P = 0.0007$) and the standard deviation ($P = 0.0176$) were higher in malignant breasts (**Figure 7a**), which suggests a strong variation in tissue signals potentially due to the growth of microvasculature. These results are consistent with our earlier reports in the DSM system [29] and indicate that the OneTouch setup can be used to differentiate healthy breasts and tumor-bearing breasts.

Moreover, we analyzed the tumor-bearing breast tissue on different breast densities. In **Figure 7b**, the heterogeneous breast exhibited slightly higher average intensity and vessel intensity compared to the scattered fibroglandular breast (extremely dense breast cases were excluded as only 2 cases were available). This difference highlights the greater vascular complexity and density in malignant heterogeneously dense

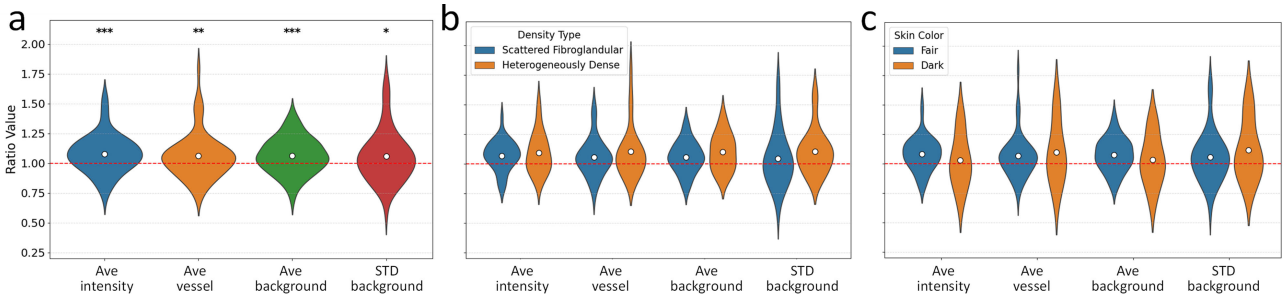

Fig. 7. Statistical analysis of PA signal intensity in malignant and contralateral healthy breast. a. Violin plot of relative (ratio of malignant and healthy) PA intensity in 61 patients on the regional intensity, background, STD background, and the AVE vessels. (***: $p < 0.001$, **: $p < 0.01$, *: $p < 0.05$ for upper-tailed t-test). The white dots represent the mean value. b. The relative PA intensity comparison between heterogeneously dense breast (n = 23) and scatter fibroglandular breast (n = 35). c. The relative PA intensity comparison between fair color (n = 49) and dark color breasts (n = 8).

TABLE II
SUMMARY OF QUANTITATIVE PA PARAMETERS

Name	Explanation
Ave Intensity	Average PA intensity within the whole breast.
Ave Vessel	Average PA intensity within the segmented vessel region.
Ave Background	Average PA intensity within the non-vessel region.
STD Background	Standard deviation of the PA intensity within the non-vessel region.

tissue. This observation agrees with studies reporting that angiogenesis-related proteins are upregulated in dense breast tissue [47].

As PA imaging is sensitive to skin color, we made a comparison plot based on skin tone (**Figure 7c**). As we do not have sufficient cases of medium skin tone, we only compared fair and dark skin cases. It can be seen that the average PA intensity ratio is slightly lower in the darker tone cases, indicating that the background skin signals might have reduced the contrast between malignant and healthy breasts. However, the mean vessel ratio is slightly higher in the dark cases, indicating that once all the background signals were removed, the vessel contrast would still stand out. This result highlights the importance of skin effect compensation in PA breast imaging [48].

It should be noted that while we observed a slight difference in the above-mentioned mean ratios, we did not observe a statistically significant difference between the two breast density or skin color groups. These results indicate that the PA technology is not sensitive to these effects.

Besides quantification of the PA signal intensity, we also analyzed the vessel branching points. This investigation was performed on the 3D Unet processed data, which improved image resolution and vessel continuity. We noticed that the tumor-bearing breast exhibited higher average branching point density (49.1/100 cm^2) than the contralateral healthy patient (38.2/100 cm^2) ($P < 0.005$). This observation is consistent with the previous reports from Yamaga et al. [49], [50], who observed 31.7 and 27.0/100 cm^2 density for malignant and healthy tissue, respectively. However, our overall density is higher. We believe the difference in system resolution and branching point quantification methods induced this difference. In particular, the previous report relied on an operator to manually count the branching point, while our method is completely automated, enabling the detection of subtle vessels and corresponding branching points that can be difficult to distinguish with unaided eyes.

IV. DISCUSSION

In this study, we developed and evaluated the performance of a new PA/US breast imaging system, OneTouch-PAT. Compared to DSM, the new system offers better patient comfort and higher ultrasound image quality. In addition, we utilized deep learning techniques to enhance the visualization of breast vasculature. The OneTouch can image the vasculature of the breast at a depth of 3 cm with a field of view of 15 × 17 cm^2. The PA and US images from OneTouch-PAT were combined and compared to clinical ultrasound images to localize the tumor site. Representative results from five patients were highlighted to demonstrate the advantage of 3D imaging. In most cases, we noticed blood vessels surrounding the tumor run irregularly, which are characteristics of tumor neovascularization.

Compared to handheld PA-US breast imaging systems, the automated breast scanning removed the operator dependence and provided a more comprehensive view of the breast vasculature. As can be seen in Figures 4-6, the cross-sectional view can only reveal limited vascular information, while the 3D view provides complete vasculature around the malignant lesion. By sectioning across the suspicious regions, we can get a complete picture of the morphological information of the lesion using US. The tumor shapes and structure agree with typical findings in the US regarding tumor subtypes [51], while the addition of PA vasculature provides additional functional information. Our case studies indicated that the most significant image pattern associated with LUMA and LUMB malignancies was the presence of feeding vessels. On the other hand, TNBC malignancies were observed with spotty signals in the tumoral region. This may be partially attributed to the lack of ER and HER2 expression, which is associated with diminished angiogenic signaling and a less organized vascular architecture, resulting in poorly structured or fragmented vascular networks. These results agree with cross-sectional studies from a larger patient population [52], highlighting the promise of combining volumetric PA and US images for breast tumor subtype identification and personalized treatment planning.

Future studies with larger and more balanced cohorts across tumor subtypes, tumor sizes, and disease stages are necessary to validate and generalize the results.

By analyzing vascular features, regional PA signal intensity, and vessel branching complexity, we identified the differences that correlate with tumor presence. The statistical findings prove that PA imaging can serve as a potential functional imaging biomarker for breast cancer classification. Regional PA intensity was significantly higher in malignant breasts ($p = 0.0002$), supporting the hypothesis that tumor angiogenesis leads to increased hemoglobin accumulation. Vessel signal intensity in malignant regions was also significantly higher than in healthy breast tissue ($p = 0.0062$), confirming that tumor-associated vascular remodeling results in larger and denser blood vessels. Additionally, background PA intensity, measured in areas without visible vasculature, was significantly higher in malignant tissue ($p = 0.0007$), likely reflecting diffuse microvascular contribution. Breast density is an important factor affecting breast cancer detection, particularly in imaging modalities. Our findings suggest that tumor angiogenesis varies with breast density, as heterogeneously dense breasts exhibited a slightly higher PA intensity ratio (malignant vs. the contralateral healthy breast) than scattered fibroglandular breasts. As for the skin effort, we found that the quantification on vessel intensity ratio is less affected by skin color. In addition to PA intensity, we quantified vessel branching points, which provide insight into tumor vascular architecture and angiogenesis. The tumor-containing breast has a significantly higher branching point density than the contralateral healthy breast.

Although our findings support stronger vascular signals in malignant lesions compared to contralateral healthy tissues, the absence of a direct comparison with benign breast lesions limits our ability to definitively attribute increased vascular signals solely to malignancy-specific angiogenesis. In our future studies, we will recruit more benign cases and investigate whether PA can differentiate malignant and benign lesions. In addition, while most PA feature ratios are statistically larger than 1, several patient cases still exhibit a malignant-healthy ratio of less than 1. These indicates the need to explore other PA features or combine both PA and US markers for more accurate tumor identification. A comprehensive classification framework leveraging quantitative PA and US imaging parameters would provide higher accuracy in cancer identification, as demonstrated in our preliminary study in dual-modal data analysis [53]. Ultimately, we hope not only to identify the breast that contains the tumor, but also accurately localize the tumor position in that breast.

While the prototype system has highlighted the advantage of PA in breast imaging, additional hardware improvements can also be implemented to further improve system performance. For instance, the current setup is limited to a single laser wavelength due to space limitations. Adding another wavelength will provide functional information of breast tissue and offer more details for pathological analysis, such as malignancy-induced tissue oxygenation change [54], [55]. This information cannot be obtained by Doppler US or ultra-fast vascular ultrasound [50]. In addition, our current transducer has only 128 elements and a round trip scanning is needed. Expanding the element number to 256 elements or higher will reduce the imaging time to less than 30 seconds. The higher element count will also enable higher ultrasound frequency (due to smaller elements) and offer better ultrasound imaging quality [56]. Finally, although our current setup achieves imaging depths of up to 3 cm, deeper lesions—such as those in ILC—may require greater penetration. Replacing the coupling water with a medium that has lower optical attenuation could further enhance imaging depth and improve visualization of structures near the chest wall.

V. Conclusion

In summary, we proposed an automated PA&US system that images patients in the standing pose. Compared to X-ray mammogram, the OneTouch-PAT system does not require painful compression and the sensitivity does not degrade in dense breast tissue. Compared to MRI, the system does not require radiation or contrast injection, and it is not as expensive or time-consuming. Given the automated scanning nature, operator variability is almost negligible in OneTouch-PAT system compared to handheld ultrasound. We also developed a data processing approach for better processing of PA data and enhancement of vascular features. The combination of the hardware and software design allows OneTouch-PAT to provide co-registered PA and US images in 3D. US provides morphological features of the breast, while the PA overlay shows the vascular patterns around the tumor, potentially providing more accurate classification of tumor grade and subtypes. Our results also demonstrated that PA imaging provides statistically significant differences in signal intensity and vessel distribution between malignant and healthy breast tissues. These results highlight the potential of PA as a complementary tool for diagnostic breast cancer imaging. Future work will focus on expanding the patient number and refining PA feature extraction methods to further enhance the clinical utility of this technology into screening applications.

References

[1] *Breast Cancer Source: Globocan*, W.H. Org., Geneva, Switzerland, 2020.
[2] B. S. Chhikara and K. Parang, "Global cancer statistics 2022: The trends projection analysis," *Chem. Biol. Lett.*, vol. 10, no. 1, p. 451, 2023.
[3] R. A. Smith et al., "Cancer screening in the United States, 2019: A review of current American cancer society guidelines and current issues in cancer screening," *CA, A Cancer J. Clinicians*, vol. 69, no. 3, pp. 184–210, May 2019.
[4] M. S. Bae et al., "Breast cancer detected with screening U.S.: Reasons for nondetection at mammography," *Radiology*, vol. 270, no. 2, pp. 369–377, Feb. 2014.
[5] R. W. Pinsky and M. A. Helvie, "Mammographic breast density: Effect on imaging and breast cancer risk," *J. Nat. Comprehensive Cancer Netw.*, vol. 8, no. 10, pp. 1157–1165, Oct. 2010.
[6] B. M. Haas, V. B. Kalra, J. Geisel, M. Raghu, M. A. Durand, and L. E. Philpotts, "Comparison of tomosynthesis plus digital mammography and digital mammography alone for breast cancer screening," *Radiology*, vol. 269, no. 3, pp. 694–700, Jul. 2013.
[7] M. S. Jochelson and M. B. I. Lobbes, "Contrast-enhanced mammography: State of the art," *Radiology*, vol. 299, no. 1, pp. 36–48, Apr. 2021.
[8] C. K. Kuhl et al., "Mammography, breast ultrasound, and magnetic resonance imaging for surveillance of women at high familial risk for breast cancer," *J. Clin. Oncol.*, vol. 23, no. 33, pp. 8469–8476, Nov. 2005.

[9] A. Grubstein, M. Yepes, and R. Kiszonas, "Magnetic resonance imaging of breast vascularity in medial versus lateral breast cancer," *Eur. J. Radiol.*, vol. 75, no. 2, pp. e9–e11, Aug. 2010.

[10] R. F. Brem et al., "Assessing improvement in detection of breast cancer with three-dimensional automated breast US in women with dense breast tissue: The SomoInsight study," *Radiology*, vol. 274, no. 3, pp. 663–673, Mar. 2015.

[11] K. Kratkiewicz, A. Pattyn, N. Alijabbari, and M. Mehrmohammadi, "Ultrasound and photoacoustic imaging of breast cancer: Clinical systems, challenges, and future outlook," *J. Clin. Med.*, vol. 11, no. 5, p. 1165, Feb. 2022.

[12] L. Lin and L. V. Wang, "The emerging role of photoacoustic imaging in clinical oncology," *Nature Rev. Clin. Oncol.*, vol. 19, no. 6, pp. 365–384, Jun. 2022.

[13] L. V. Wang and S. Hu, "Photoacoustic tomography: In vivo imaging from organelles to organs," *Science*, vol. 335, no. 6075, pp. 1458–1462, Mar. 2012.

[14] R. A. Kruger et al., "Dedicated 3D photoacoustic breast imaging," *Med. Phys.*, vol. 40, no. 11, 2013, Art. no. 113301.

[15] A. G. Bell, "On the production and reproduction of sound by light," *Amer. J. Sci.*, vols. s3–20, no. 118, pp. 305–324, Oct. 1880.

[16] P. Beard, "Biomedical photoacoustic imaging," *Interface Focus*, vol. 1, no. 4, pp. 602–631, Jun. 2011.

[17] A. C. Tam, "Applications of photoacoustic sensing techniques," *Rev. Modern Phys.*, vol. 58, no. 2, pp. 381–431, Apr. 1986.

[18] W. Choi et al., "Three-dimensional multistructural quantitative photoacoustic and US imaging of human feet in vivo," *Radiology*, vol. 303, no. 2, pp. 467–473, May 2022.

[19] R. A. Kruger, R. B. Lam, D. R. Reinecke, S. P. Del Rio, and R. P. Doyle, "Photoacoustic angiography of the breast," *Med. Phys.*, vol. 37, no. 11, pp. 6096–6100, Nov. 2010.

[20] V. Periyasamy, N. Das, A. Sharma, and M. Pramanik, "1064 nm acoustic resolution photoacoustic microscopy," *J. Biophotonics*, vol. 12, no. 5, May 2019, Art. no. e201800357.

[21] N. Nyayapathi et al., "Dual scan mammoscope (DSM)—A new portable photoacoustic breast imaging system with scanning in craniocaudal plane," *IEEE Trans. Biomed. Eng.*, vol. 67, no. 5, pp. 1321–1327, May 2020.

[22] J. Park et al., "Clinical translation of photoacoustic imaging," *Nature Rev. Bioengineering*, vol. 3, no. 3, pp. 193–212, Sep. 2024.

[23] S. Manohar and M. Dantuma, "Current and future trends in photoacoustic breast imaging," *Photoacoustics*, vol. 16, Dec. 2019, Art. no. 100134.

[24] C. G. A. Hoelen, F. F. M. de Mul, R. Pongers, and A. Dekker, "Three-dimensional photoacoustic imaging of blood vessels in tissue," *Opt. Lett.*, vol. 23, no. 8, p. 648, Apr. 1998.

[25] S. R. McDougall, A. R. A. Anderson, and M. A. J. Chaplain, "Mathematical modelling of dynamic adaptive tumour-induced angiogenesis: Clinical implications and therapeutic targeting strategies," *J. Theor. Biol.*, vol. 241, no. 3, pp. 564–589, Aug. 2006.

[26] D. R. Bielenberg and B. R. Zetter, "The contribution of angiogenesis to the process of metastasis," *Cancer J.*, vol. 21, no. 4, pp. 267–273, Jul. 2015.

[27] A. A. Oraevsky, B. Clingman, J. Zalev, A. T. Stavros, W. T. Yang, and J. R. Parikh, "Clinical optoacoustic imaging combined with ultrasound for coregistered functional and anatomical mapping of breast tumors," *Photoacoustics*, vol. 12, pp. 30–45, Dec. 2018.

[28] L. Lin et al., "Single-breath-hold photoacoustic computed tomography of the breast," *Nature Commun.*, vol. 9, no. 1, p. 2352, Jun. 2018.

[29] N. Nyayapathi et al., "Photoacoustic dual-scan mammoscope: Results from 38 patients," *Biomed. Opt. Exp.*, vol. 12, no. 4, p. 2054, Apr. 2021.

[30] S. Mallidi, G. P. Luke, and S. Emelianov, "Photoacoustic imaging in cancer detection, diagnosis, and treatment guidance," *Trends Biotechnol.*, vol. 29, no. 5, pp. 213–221, May 2011.

[31] L. Lin, X. Tong, P. Hu, M. Invernizzi, L. Lai, and L. V. Wang, "Photoacoustic computed tomography of breast cancer in response to neoadjuvant chemotherapy," *Adv. Sci.*, vol. 8, no. 7, Apr. 2021, Art. no. 2003396.

[32] N. Nyayapathi and J. Xia, "Photoacoustic imaging of breast cancer: A mini review of system design and image features," *J. Biomed. Opt.*, vol. 24, no. 12, p. 1, Nov. 2019.

[33] S. M. Schoustra et al., "Twente photoacoustic mammoscope 2: System overview and three-dimensional vascular network images in healthy breasts," *J. Biomed. Opt.*, vol. 24, no. 12, p. 1, Oct. 2019.

[34] Y. Matsumoto et al., "Visualising peripheral arterioles and venules through high-resolution and large-area photoacoustic imaging," *Sci. Rep.*, vol. 8, no. 1, p. 14930, Oct. 2018.

[35] A. Oraevsky et al., "Full-view 3D imaging system for functional and anatomical screening of the breast," *Proc. SPIE*, vol. 10494, pp. 217–226, Apr. 2018.

[36] K. Stephens, "FDA approves seno medical's breast cancer diagnostic technology," in *AXIS Imaging News; Overland Park*, Jan. 2021.

[37] E. Zheng, H. Zhang, S. Goswami, I. E. Kabir, M. M. Doyley, and J. Xia, "Second-generation dual scan mammoscope with photoacoustic, ultrasound, and elastographic imaging capabilities," *Frontiers Oncol.*, vol. 11, Nov. 2021, Art. no. 779071.

[38] Y. Wang, R. S. A. Lim, H. Zhang, N. Nyayapathi, K. W. Oh, and J. Xia, "Optimizing the light delivery of linear-array-based photoacoustic systems by double acoustic reflectors," *Sci. Rep.*, vol. 8, no. 1, pp. 1–7, Aug. 2018.

[39] F. C. Delori, R. H. Webb, and D. H. Sliney, "Maximum permissible exposures for ocular safety (ANSI 2000), with emphasis on ophthalmic devices," *J. Opt. Soc. Amer. A, Opt. Image Sci.*, vol. 24, no. 5, p. 1250, May 2007.

[40] Y. Wang, Y. Zhan, M. Tiao, and J. Xia, "Review of methods to improve the performance of linear array-based photoacoustic tomography," *J. Innov. Opt. Health Sci.*, vol. 13, no. 2, Mar. 2020, Art. no. 2030003.

[41] H. Zhang et al., "Deep-E: A fully-dense neural network for improving the elevation resolution in linear-array-based photoacoustic tomography," *IEEE Trans. Med. Imag.*, vol. 41, no. 5, pp. 1279–1288, May 2022.

[42] W. Zheng et al., "Deep learning enhanced volumetric photoacoustic imaging of vasculature in human," *Adv. Sci.*, vol. 10, no. 29, Oct. 2023, Art. no. 2301277.

[43] J.-Y. Zhu, H.-L. He, X.-C. Jiang, H.-W. Bao, and F. Chen, "Multimodal ultrasound features of breast cancers: Correlation with molecular subtypes," *BMC Med. Imag.*, vol. 23, no. 1, p. 57, Apr. 2023.

[44] D. Ribatti, B. Nico, S. Ruggieri, R. Tamma, G. Simone, and A. Mangia, "Angiogenesis and antiangiogenesis in triple-negative breast cancer," *Translational Oncol.*, vol. 9, no. 5, pp. 453–457, Oct. 2016.

[45] E. Neuschler et al., "A pivotal study of optoacoustic imaging to diagnose benign and malignant breast masses: A new evaluation tool for radiologists," *Radiology*, vol. 287, no. 2, pp. 398–412, Nov. 2017.

[46] A. E. Becker et al., "Multispectral optoacoustic tomography of the human breast: Characterisation of healthy tissue and malignant lesions using a hybrid ultrasound-optoacoustic approach," *Eur. Radiol.*, vol. 28, no. 2, pp. 602–609, Aug. 2017.

[47] P. Lundberg, M. Forsgren, J. Tellman, J. Kihlberg, A. Rzepecka, and C. Dabrosin, "Breast density is strongly associated with multiparametric magnetic resonance imaging biomarkers and pro-tumorigenic proteins in situ," *Brit. J. Cancer*, vol. 127, no. 11, pp. 2025–2033, Sep. 2022.

[48] C. Huang et al., "Enhanced clinical photoacoustic vascular imaging through a skin localization network and adaptive weighting," *Photoacoustics*, vol. 42, Jan. 2025, Art. no. 100690.

[49] I. Yamaga et al., "Vascular branching point counts using photoacoustic imaging in the superficial layer of the breast: A potential biomarker for breast cancer," *Photoacoustics*, vol. 11, pp. 6–13, Sep. 2018.

[50] J. Gu et al., "Volumetric imaging and morphometric analysis of breast tumor angiogenesis using a new contrast-free ultrasound technique: A feasibility study," *Breast Cancer Res.*, vol. 24, no. 1, p. 85, Nov. 2022.

[51] L. M. R. Khalaf and R. A. Herdan, "Role of ultrasound in predicting the molecular subtypes of invasive breast ductal carcinoma," *Egyptian J. Radiol. Nucl. Med.*, vol. 51, no. 1, pp. 1–9, Dec. 2020.

[52] B. E. Dogan et al., "Stavros, optoacoustic imaging and gray-scale US features of breast cancers: Correlation with molecular subtypes," *Radiology*, vol. 292, no. 3, pp. 564–572, 2019.

[53] E. Zheng, H. Zhang, E. Bonaccio, K. Takabe, W. Xu, and J. Xia, "Co-registered photoacoustic and ultrasound imaging with deep learning for breast imaging and tumor localization," in *Frontiers in Optics + Laser Science 2024 (FiO, LS)* (Technical Digest Series). Optica Publishing Group, 2024, pp. 1–2, Paper JW5A.19.

[54] Z. Huang et al., "Assessment of oxygen saturation in breast lesions using photoacoustic imaging: Correlation with benign and malignant disease," *Clin. Breast Cancer*, vol. 24, no. 4, pp. e210–e218, Jan. 2024.

[55] R. Butler et al., "Makariou, optoacoustic breast imaging: Imaging-pathology correlation of optoacoustic features in benign and malignant breast masses," *Amer. J. Roentgenology*, vol. 211, no. 5, pp. 1155–1170, 2018.

[56] S. Park et al., "Simultaneous multispectral photoacoustic and ultrasound 3D automated breast scanner for breast cancer detection," *Proc. SPIE*, vol. 13319, pp. 77–82, Mar. 2025.